



Article

3D-Structured Au(NiMo)/Ti Catalysts for the Electrooxidation of Glucose

Aldona Balčiūnaitė *, Daina Upskuvienė, Augustas Antanaitis, Dijana Šimkūnaitė, Loreta Tamašauskaitė-Tamašiūnaitė , Jūratė Vaičiūnienė and Eugenijus Norkus 

Center for Physical Sciences and Technology (FTMC), Saulėtekio Ave. 3, LT-10257 Vilnius, Lithuania

* Correspondence: aldona.balciunaite@ftmc.lt

Abstract: In this study, 3D-structured NiMo coatings have been constructed via the widely used electrodeposition method on a Ti surface and decorated with very small Au crystallites by galvanic displacement (Au(NiMo)/Ti). The catalysts have been characterized using scanning electron microscopy, energy dispersive X-ray analysis, and inductively coupled plasma optical emission spectroscopy. Different Au(NiMo)/Ti catalysts, which had Au loadings of 1.8, 2.3, and 3.9 $\mu\text{g}_{\text{Au}} \text{cm}^{-2}$, were prepared. The electrocatalytic activity of the Au(NiMo)/Ti catalysts was examined with respect to the oxidation of glucose in alkaline media by cyclic voltammetry. It was found that the Au(NiMo)/Ti catalysts with Au loadings in the range of 1.8 up to 3.9 $\mu\text{g}_{\text{Au}} \text{cm}^{-2}$ had a higher activity compared to that of NiMo/Ti. A direct glucose-hydrogen peroxide ($\text{C}_6\text{H}_{12}\text{O}_6\text{-H}_2\text{O}_2$) single fuel cell was constructed with the different Au-loading-containing Au(NiMo)/Ti catalysts as the anode and Pt as the cathode. The fuel cells exhibited an open circuit voltage of ca. 1.0 V and peak power densities up to 8.75 mW cm^{-2} at 25 °C. The highest specific peak power densities of 2.24 $\text{mW } \mu\text{g}_{\text{Au}}^{-1}$ at 25 °C were attained using the Au(NiMo)/Ti catalyst with the Au loading of 3.9 $\mu\text{g cm}^{-2}$ as the anode.



Citation: Balčiūnaitė, A.; Upskuvienė, D.; Antanaitis, A.; Šimkūnaitė, D.; Tamašauskaitė-Tamašiūnaitė, L.; Vaičiūnienė, J.; Norkus, E. 3D-Structured Au(NiMo)/Ti Catalysts for the Electrooxidation of Glucose. *Catalysts* **2022**, *12*, 892. <https://doi.org/10.3390/catal12080892>

Academic Editor: Yongjun Feng

Received: 19 July 2022

Accepted: 12 August 2022

Published: 13 August 2022

Publisher's Note: MDPI stays neutral with regard to jurisdictional claims in published maps and institutional affiliations.



Copyright: © 2022 by the authors. Licensee MDPI, Basel, Switzerland. This article is an open access article distributed under the terms and conditions of the Creative Commons Attribution (CC BY) license (<https://creativecommons.org/licenses/by/4.0/>).

Keywords: gold; nickel; molybdenum; titanium; anode catalyst; glucose oxidation

1. Introduction

Fuel cells based on glucose fuel have received a lot of attention because of their application in various regions, such as glucose biofuel cells (GBFCs) for powering medical implants [1–3], bioelectricity, and treating wastewater [4]. Glucose is a perfect choice of biofuel that can be effectively converted to electrical energy and which often improves the functional parameters of the biofuel cell or simply allows the use of cheaper fuels. Noble metals and their alloys are constantly applied for electrochemical glucose oxidation (GOR) in connection with their considerable response and splendid selectivity [5–9]. Nevertheless, the high cost of these raw materials hinders their wider application. This gives rise to the desire and need to develop low-cost and high-performance GOR catalysts [10]. On the whole, Ni and Ni-based catalysts [11–24], Mo and Mo-based composites [15,18,21,24,25], Cu [12,25,26], Co [11,16,19,20,27–29], and other transition metals, due to their high catalytic activities and reasonable cost, presented good electrocatalytic activity to glucose oxidation reaction in alkaline solutions, none the worse than Pt or Au. The monometallic species (Ni, Mo, Co, Cu, etc.) can be used as catalysts for GOR, but bimetallic catalysts, such as NiMo [24], CuMo [25], BiMo [30], NiCo [11,16,19,20], etc., exhibited better catalytic activities compared to those of monometallic catalysts due to their unique synergistic contribution.

Recently, the development of three-dimensional (3D) nanomaterials has attracted a great deal of research interest [22,28,29,31–34] due to their sufficiently high surface area to volume ratio and a high percentage of exposed atoms, as electrochemical reactions generally take place at surfaces or interfaces. Considerable surface areas of 3D nanomaterials render large space for electrostatic ion adsorption to reach considerable electrical bilayer capacities [35,36]. The nanoporous three-dimensional catalysts can be synthesized in a

variety of different ways, including template synthesis [37–40], surfactant-mediated synthesis [41,42], dealloying [43], etc. Among them, electrodeposition is a convenient one for large area deposition; it is an inexpensive, effective, simple, and readily adaptable method when compared with most physical methods. Recently, the dynamic hydrogen bubble template (DHBT) technique has been successfully applied for producing nanoporous structures of monometallic catalysts, such as Au [44,45] and Ni [46], bimetallics, such as Cu-Au [47] and Ni-Cu [48], and various multimetallics, such as the Pt-Ni-Cu [49] catalyst. The high cathodic current densities employed during electrodeposition resulted in a continuous bubbling of H₂, which limited the free volume available for metal growth by blocking the diffusion of active species, giving rise to three-dimensional coating-like morphologies with randomly distributed micrometric and nanometric pores obtained under mass transfer conditions [50].

In this study, we suggest using 3D-structured Ni, Mo, and NiMo coatings decorated with a small amount of Au crystallites for GOR. The three-dimensional coatings modified with noble metal crystallites are a reasonably good choice because they would present a good electrocatalytic effect, extra conductivity, and high catalytic activity from noble metal and metal coatings. To prove this idea, we synthesized Au nanoparticles supported on the Ni/Ti, Mo/Ti, and NiMo/Ti composites with the 3D structure. Of the conventional precious metals, Au was chosen because of its extremely stable conductive properties and good catalytic activity [5,8,9]. The adjunction of Na₂MoO₄ appreciably affects the coating appearance and thickness. Molybdate anions are non-toxic and environmentally friendly. They were chosen as a conceivable alteration to toxicity ions such as nitrite and chromate in aqueous systems. By forming insoluble complexes on the metal surface, they adsorb to the interface of the metal solution [51]. The Ni- or Mo-based coatings, decorated with Au nanoparticles coatings, have durable, inexpensive, and meaningful electrochemical activity in an alkaline environment, serving as up-and-coming candidates for electrochemical needs. Based on the anodic and cathodic electrochemical characterization, it can be argued that the porous Ni-Mo coatings deposited on the Ti base and decorated with Au nanoparticles are an efficacious and durable trifunctional electrocatalyst directed to GOR in an alkaline medium.

2. Results and Discussion

2.1. Characterization of Coatings

This study presents the preparation of 3D-structured Ni, Mo, and NiMo coatings using the DHBT technique, followed by their decoration with a very small amount of Au crystallites by galvanic displacement and their application for the electrooxidation of glucose. Ni, Mo, and NiMo coatings were electrochemically deposited on the Ti surface using cathodic currents at sufficiently negative potentials related to a vigorous H₂ bubbling. The release of H₂ bubbles from the substrate interrupts the local growth of metals, creating a dynamic template for the preparation of porous coatings. The morphology and composition of the prepared Ni/Ti, Au(Ni)/Ti, Mo/Ti, Au(Mo)/Ti, NiMo/Ti, and Au(NiMo)/Ti catalysts have been characterized by SEM, EDX, and ICP-OES techniques and are presented in Figures 1 and 2 and Table 1. SEM images for the Mo and Ni coatings given at different magnifications clearly show that obtained patterns differ greatly in shape. The Mo coating surface is smooth and almost without any obvious distinctive features as evident from SEM images in Figure 1a. In contrast, the Ni coating produces a well-defined open-porous network structure with interconnected fibers composed of spherical particles in sizes of 240–620 nm (Figure 1b). The decoration of both coatings with Au crystallites using the galvanic displacement technique seems to give a more pronounced porous architecture in both cases (Figure 1c,d). In the case of the AuMo coating, dark spots appear, reflecting spatial cavities of ca 0.4–1.5 μm in size (Figure 1c). Meanwhile, in the case of AuNi, the spherical particles tend to agglomerate into ca. 1.0–1.7 μm-sized particles (Figure 1d). The elemental composition of those porous structures can be clearly revealed by the corresponded EDX spectra of the elements (Figure 1e,f) and ICP-OES analysis (Table 1). The data obtained confirm the presence of Au, Mo, and Ni in the above-mentioned catalysts coatings.

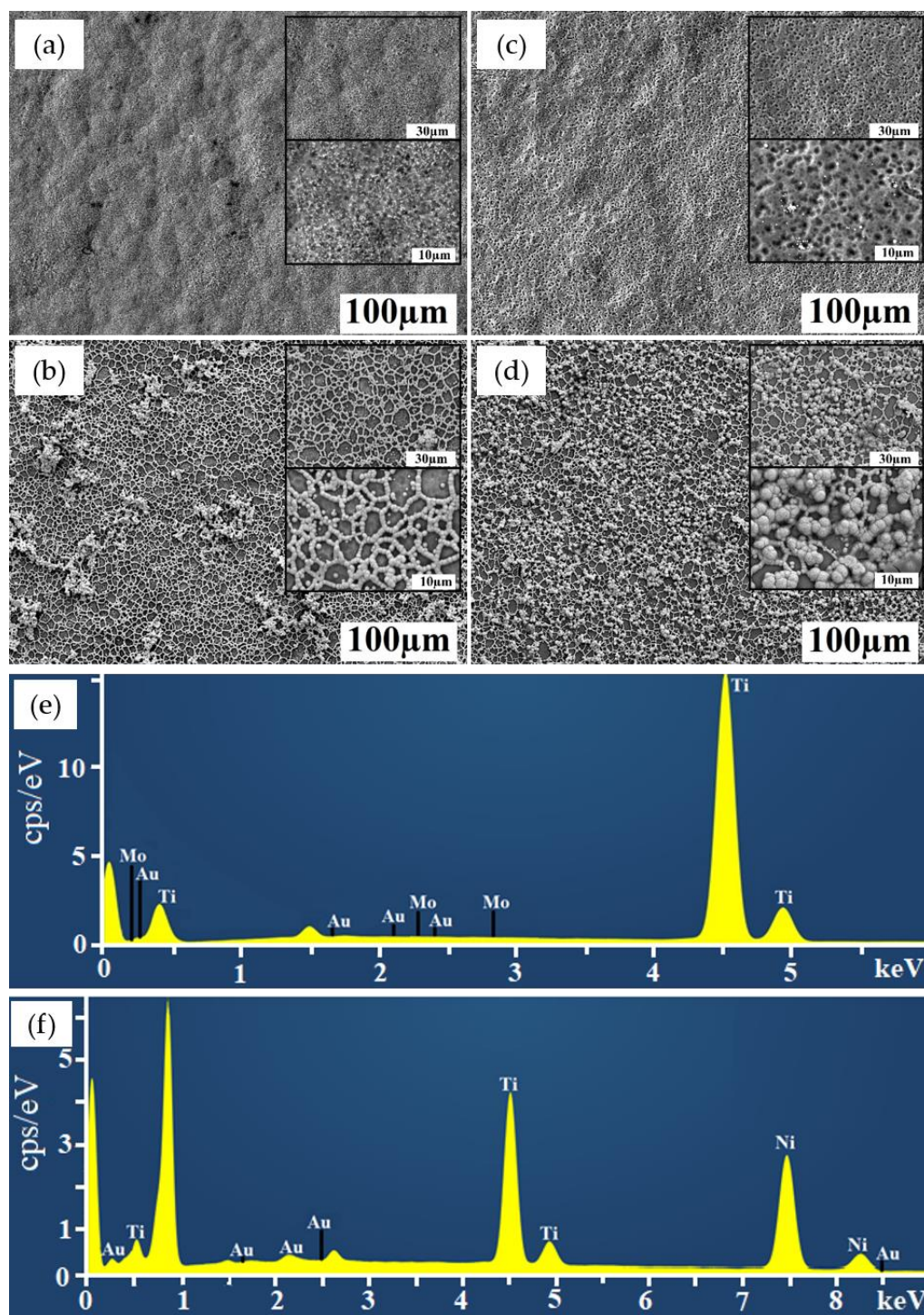


Figure 1. SEM images of Mo/Ti (a), Ni/Ti (b), Au(Mo)/Ti (c), and Au(Ni)/Ti (d) coatings. The corresponded EDX spectra of Au(Mo)/Ti (e) and Au(Ni)/Ti (f) coatings.

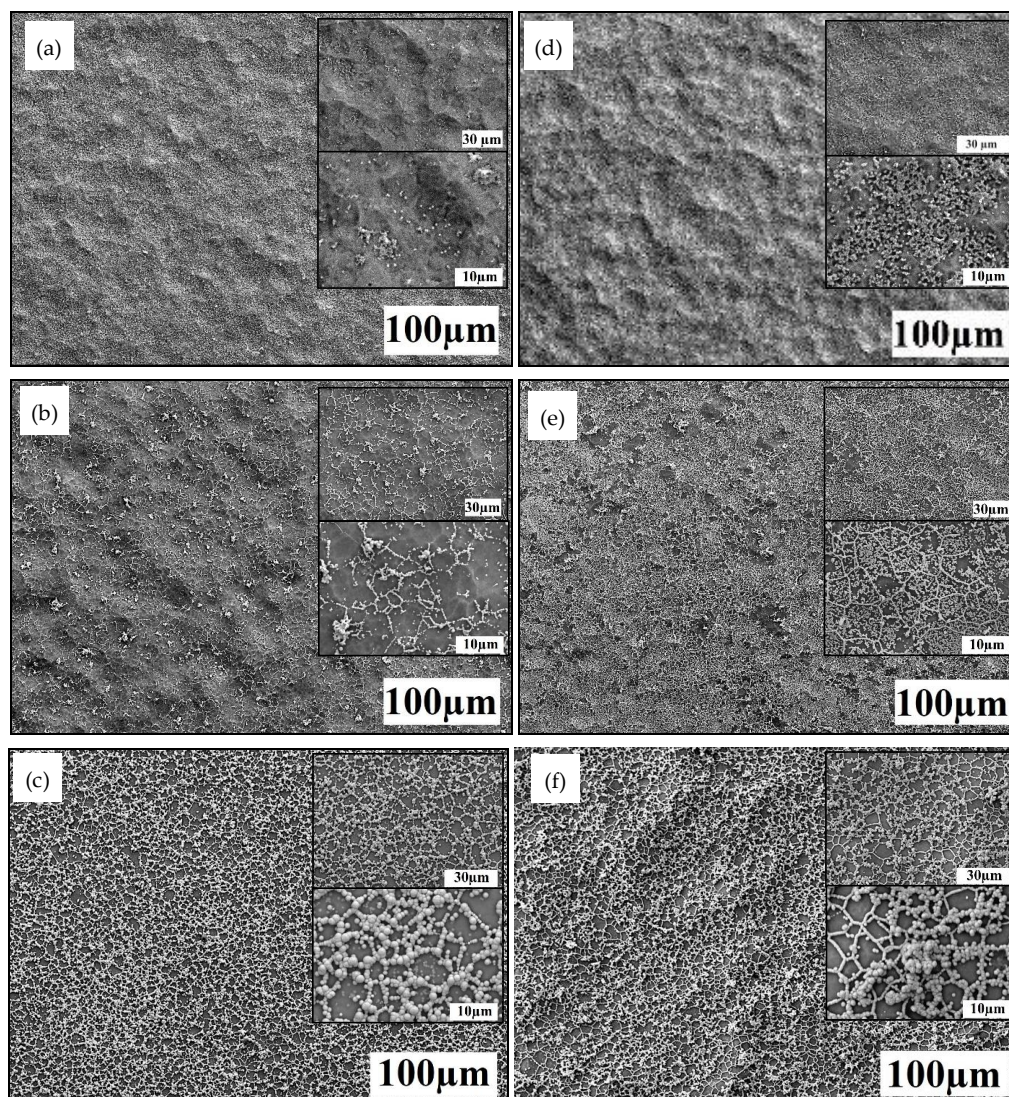


Figure 2. SEM images of NiMo/Ti-1 (a), NiMo/Ti-2 (b), NiMo/Ti-3 (c), Au(NiMo)/Ti-1 (d), Au(NiMo)/Ti-2 (e), and Au(NiMo)/Ti-3 (f) coatings.

Table 1. The composition of coatings by ICP-OES.

Catalyst	Ni, Loadings $\mu\text{gNi cm}^{-2}$	Mo, Loadings $\mu\text{gMo cm}^{-2}$	Au, Loadings $\mu\text{gAu cm}^{-2}$	Total Metal Loading ($\mu\text{g cm}^{-2}$)
Ni/Ti	96.5	-	-	96.5
Mo/Ti	-	6.5	-	6.5
NiMo/Ti-1	13.5	2.1	-	15.6
NiMo/Ti-2	35.7	4.3	-	40.0
NiMo/Ti-3	39.3	5.7	-	45.0
Au(Ni)/Ti	59.9	-	4.1	64.0
Au(Mo)/Ti	-	4.1	1.2	5.3
Au(NiMo)/Ti-1	11.7	1.9	1.8	15.4
Au(NiMo)/Ti-2	32.9	3.8	2.3	39.0
Au(NiMo)/Ti-3	34.1	4.5	3.9	42.5

Figure 2a–c show the SEM images of the NiMo layer electrodeposited on the Ti surface as a function of the $\text{Ni}^{2+}/\text{Mo}^{6+}$ ratio of the plating solutions listed in Table 4 (in Sections 3 and 3.2, Fabrication of catalysts), which was varied by changing the concentration

of NiSO_4 , while the concentration of Na_2MoO_4 was kept constant. Compositions of the analyzed coatings as a function of the $\text{Ni}^{2+}/\text{Mo}^{6+}$ ratio are presented in Table 1. Figure 2a shows randomly distributed spherical particles of 215–460 nm in size for the $\text{Ni}^{2+}/\text{Mo}^{6+}$ ratio of 1, generating ca. 6.8 times higher Ni loading compared to that of Mo ((NiMo)/Ti-1). Increasing the $\text{Ni}^{2+}/\text{Mo}^{6+}$ ratio to 10 or 5 produces 8.3 and 6.9 times higher Ni loadings compared with that of Mo, respectively, resulting in the development of Ni-Mo layers on the Ti surface ((NiMo)/Ti-2 and (NiMo)/Ti-3) with a well-defined porous structure (Figure 2b,c). It is obvious that the concentration of Ni^{2+} ions determines the formation of porous coatings with only a tiny contribution from Mo.

Modification of the above-mentioned (NiMo)/Ti-1, (NiMo)/Ti-2, and (NiMo)/Ti-3 catalysts with low Au loadings ranging from 1.8 to $3.9 \mu\text{g}_{\text{Au}} \text{cm}^{-2}$ gives quite similar but more densely packed SEM views (Figure 2e,f), indicating that more pronounced porous structures are obtained when higher concentrations of Ni^{2+} ions are used for the preparation of the catalysts. Nevertheless, the diameters of the fibers observed in both Au(NiMo)/Ti-2 and Au(NiMo)/Ti-3 catalysts vary considerably. However, they are still neatly joined together to form a series of macroporous channels that are responsible for more facile ion transportation. At the same time, they produce coatings with a very large surface area for electrochemical reactions. The elemental composition of these porous structures is presented by an elemental mapping in Figure 3a–c. Au, Ni, Mo, and Ti elemental signals are detected, clearly indicating their presence in the porous architecture of Au(NiMo)/Ti catalysts.

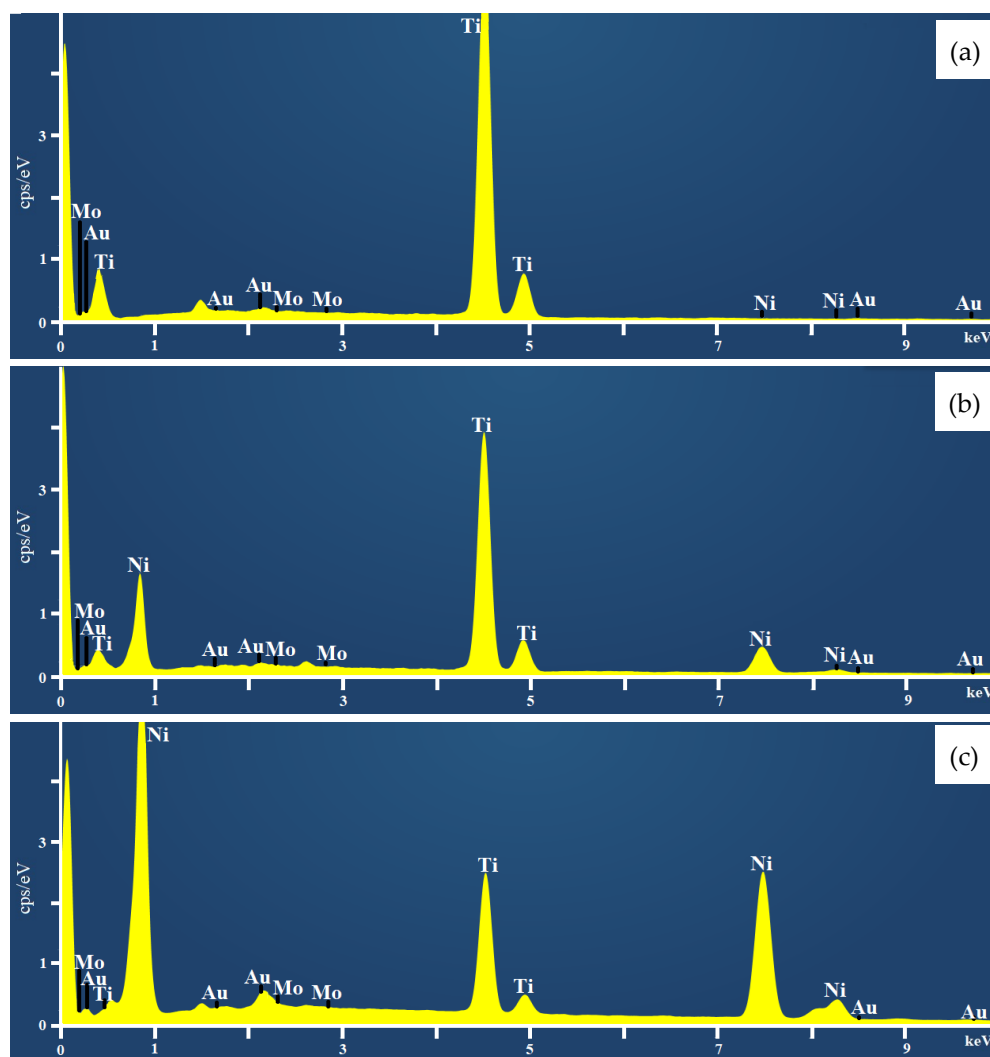


Figure 3. EDX spectra of Au(NiMo)/Ti-1 (a), Au(NiMo)/Ti-2 (b), and Au(NiMo)/Ti-3 (c) catalysts.

2.2. Electrocatalytic Activity of Catalysts for GOR

The activity of the as-prepared Ni/Ti, Mo/Ti, NiMo/Ti-1, NiMo/Ti-2, and NiMo/Ti-3 catalysts for the oxidation of glucose in an alkaline medium was evaluated using cyclic voltammetry. These synthesized catalysts were compared to that of the bare Au, Au(Ni)/Ti, Au(Mo)/Ti, Au(NiMo)/Ti-1, Au(NiMo)/Ti-2, and Au(NiMo)/Ti-3 catalysts. Figure 4 shows CVs characteristics of the bare Au electrode recorded in the 0.1 M NaOH solution (solid line) and in that containing 0.1 M glucose (dashed line) at a scan rate of 50 mV s^{-1} at a temperature of $25 \text{ }^\circ\text{C}$. The potential range was from -0.9 to 0.9 V (Ag/AgCl).

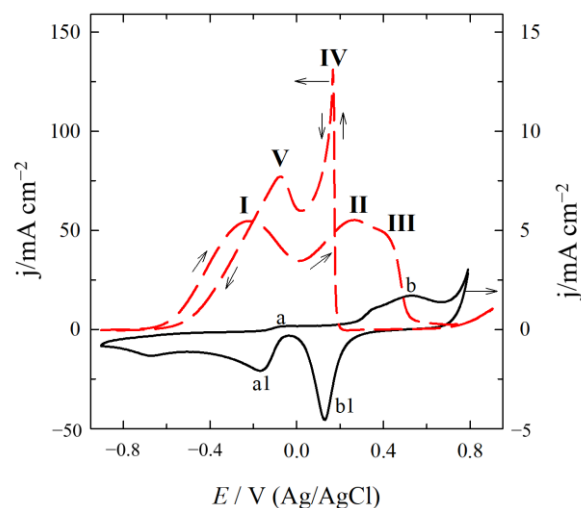


Figure 4. Stabilized CVs of the bare Au electrode recorded in the 0.1 M NaOH solution (solid line) and that containing 0.1 M glucose (dashed line) at $25 \text{ }^\circ\text{C}$ at an electrode potential scan rate of 50 mV s^{-1} .

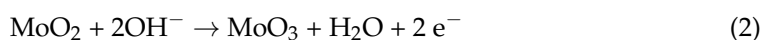
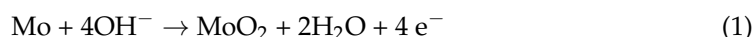
As we can see from the curves shown in Figure 4 in a 0.1 M NaOH solution, a broad oxidation peak labeled as b begins at ca. 0.25 V during the positive scan and a reduction peak labeled as b1 during the cathodic scan at ca. 0.13 V, which have corresponded to the formation of gold oxide on the surface of the bare Au electrode and its reduction, respectively. Additionally, minor redox peaks a and a1 were observed at -0.10 and -0.16 V , respectively. They are assigned to AuOH active sites formed by the chemisorption of OH^- anions in an alkaline medium [5]. The observed redox peaks indicate the continuation of uninterrupted redox reactions, which can be represented by the following continuance: $\text{Au (bare)} \leftrightarrow \text{Au (hydroxide)} \leftrightarrow \text{Au (oxide)}$. Adsorbed AuOH_{ads} formed by chemisorption of OH^- anions is considered to play a crucial role in the oxidation of glucose, especially in alkaline media where the chemisorption process is more pronounced [52–57]. It should be noted, however, that the high activity and selectivity of the 4-electron ORR pathway in the potential region starting already at low potential, around 0.00 V at the Au surface in alkaline media, cannot be excluded [58]. This is attributed to the densely packed OH_{ads} layer, which can serve as a template for ORR. At even more negative potentials, correspondingly lower OH_{ads} coverages should contribute increasingly to the 2-electron ORR pathway.

In CVs of the bare Au electrode recorded in the 0.1 M NaOH solution containing 0.1 M glucose (Figure 4, dashed line), two well-noticeable anodic oxidation peaks I, II, and barely visible peak III are observed in the positive direction. Peak I is observed at more negative potential values located at ca. -0.22 V , and peak II is observed at more positive potential values at ca. 0.25 V. Based on literature sources, those two peaks are ascribed to the oxidation of adsorbed glucose to gluconolactone [52,53,56,59,60] followed by oxidation of gluconolactone to gluconate [53,55,60,61], respectively. The barely visible peak III is observed at more positive potential values at ca. 0.45 V, the intensity of which depends on the preferential Au crystallographic plane, with the most pronounced peak value in the case of the preferential (200) plane [60]. This peak is related to the formation of a compact gold oxide layer, which results in a decrease in the amount of AuOH_{ads} ,

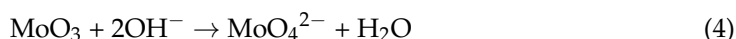
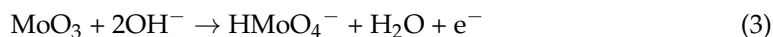
leading to a decrease in current density. It is, therefore, reasonable to assume that AuOH_{ads} influences the oxidation process of adsorbed glucose. The other two well-noticeable anodic peaks on the reverse scan, denoted as IV and V, observed at potential values of ca. 0.17 V and -0.08 V, respectively, may be ascribed to the oxidation of glucose on the renewed gold surface after gold oxide layer reduction and to the oxidation of intermediate species formed during the oxidation of glucose, respectively [53,55,56]. A comparison of the peak current densities of anodic peaks I and II shows that they are nearly equal in magnitude, supporting the probability that the gold surface is almost equally active in the oxidation of both glucose and gluconolactone. This is likely due to the presence of a sufficient amount of active AuOH_{ads} available for the oxidation process in the appropriate potential regions.

The GOR was also investigated on Mo/Ti and Ni/Ti catalysts. Electrochemical behavior of as-prepared Mo/Ti (Figure 5a) and Ni/Ti (Figure 5c) catalysts was evaluated in the background of 0.1 M NaOH aqueous solution (solid line) and in 0.1 M NaOH solution in the presence of 0.1 M glucose (dashed line) at 25 °C at a scan rate of 50 mV s⁻¹. From the CVs recorded in 0.1 M NaOH solution on the as-prepared Mo/Ti and Ni/Ti catalysts, well-defined anodic peaks b of ca. 0.77 V and 0.59 V, respectively, can be observed in the positive scan, whereas during the negative scan, only in the case of the Ni/Ti catalyst, a cathodic peak b1 of ca. 0.37 V can be noticed (Figure 5a,c). During the following cycles, both cathodic and anodic peaks remain stable in the case of the Ni/Ti catalyst and a typical current response for reversible conversion of Ni(II)/Ni(III) in alkaline media is observed. For the Mo/Ti catalyst, during the successive cycles current drops sharply and peaks disappear. Based on the Pourbaix et al. diagram [62], Mo thermodynamically is expected to dissolve in the form of highly soluble molybdate ions in alkaline media. A number of intermediate oxidation states of Mo are known to occur in the overall oxidation reaction to the final (+VI) state, but their nature is still a matter of debate [62–69].

Three different molybdenum oxide films may be identified in alkaline media between the open-circuit rest potential and the onset of steady-state oxygen evolution [64]. In the lowest potential region, $\text{MoO}_3/\text{Mo}(\text{OH})_3$ species are generated, which transform into higher valence oxidation Mo species— MoO_2 —in the intermediate potential region, converting to the final (+VI) oxidation state molybdenum species in the form of MoO_3 in the highest potential region. Therefore, the potential region from ca. -0.9 V to 0.2 V in CVs (Figure 5a) can be attributed to MoO_2 formation, which undergoes further electrochemical oxidation to MoO_3 species with a peak formation, mainly via the following reactions [64,65,67,68]:



It should be noted that electrochemically formed MoO_3 tends to dissolve to molybdate species in alkaline media that are released in solution by the following reaction [64,66,67]:



In addition, MoO_2 species are known to be unstable in aqueous solution and a parallel disproportionation reaction can proceed via the following reaction [64]:



The Above-mentioned reactions significantly contribute to the current decrease in the following cycles.

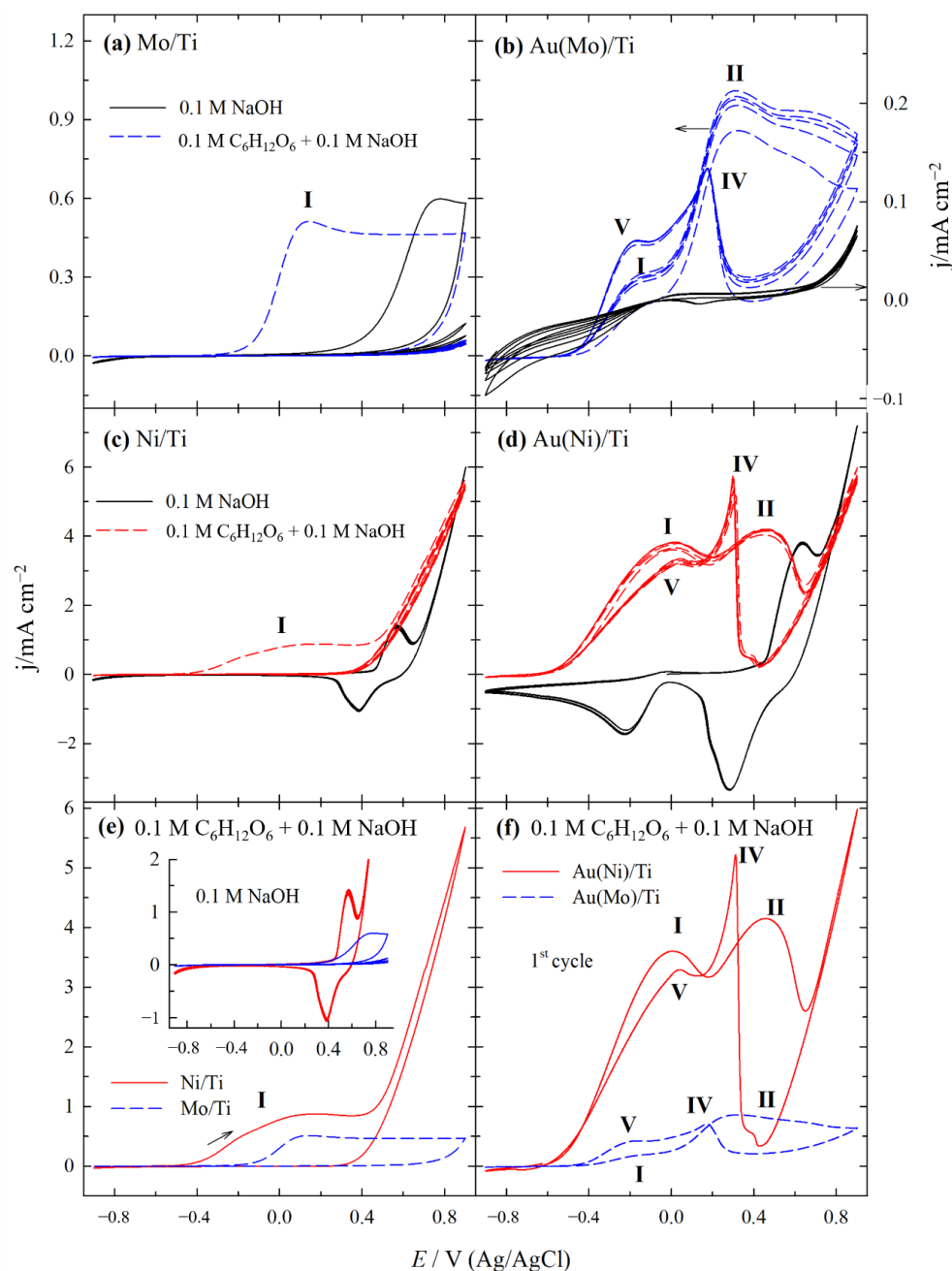


Figure 5. CVs recorded on Mo/Ti (a), Au(Mo)/Ti (b), Ni/Ti (c), and Au(Ni)/Ti (d) catalysts in the 0.1 M NaOH solution (solid line) and in that containing 0.1 M glucose (dashed line) at 25 °C at an electrode potential scan rate of 50 mV s⁻¹. First scans of CVs recorded in 0.1 M NaOH + 0.1 M $\text{C}_6\text{H}_{12}\text{O}_6$ on Ni/Ti (solid line) and Mo/Ti (dashed line) catalysts (e), and on Au(Ni)/Ti (solid line) and Au(Mo)/Ti (dashed line) catalysts (f) for the same conditions as in (a–d). The insert in (e) shows CVs recorded in 0.1 M NaOH on Ni/Ti and Mo/Ti catalysts.

Adding 0.1 M glucose to the 0.1 M NaOH solution results in higher anodic currents at more negative potential values on Ni/Ti and Mo/Ti, as compared with those obtained in the background 0.1 M NaOH solution. Broad glucose oxidation peaks start at ca. -0.49 and -0.25 V at Ni/Ti and Mo/Ti, respectively (Figure 5a,c, dashed lines). The first scans recorded on Ni/Ti and Mo/Ti catalysts (Figure 5e) clearly show that Ni/Ti outperformed the Mo/Ti catalyst. Glucose oxidation at Ni/Ti starts at more negative potential and measured current densities are higher than those at Mo/Ti. Notably, at potentials more positive than 0.4 V, significantly higher glucose oxidation current densities are observed on

the oxidized Ni surface in contrast to Mo/Ti. It should be noted that the glucose oxidation peak I on Mo/Ti and Ni/Ti catalysts was observed only in the first potential scan. During subsequent anodic scans, no appreciable increase in anodic current and no anodic peaks were observed on the Mo/Ti catalyst in the broad potential region from -0.9 to 0.9 V (Figure 5a). This indicates that the Mo/Ti catalyst is not active for GOR, mainly due to the dissolution of electrochemically formed active MoO_3 species from the substrate, since they are prone to convert into soluble molybdate species, which are released into solution during the reaction according to Equations (3) and (4). Surface poisoning by adsorbed intermediate species generated during the oxidation of glucose cannot be excluded either. In the Ni/Ti catalyst case, during subsequent anodic scans, high glucose oxidation current densities are observed at positive potentials higher than 0.4 V (Figure 5c, dashed line). Notably, at potentials higher than 0.4 V, the Ni/Ti surface is oxidized to NiOOH , whereas the clear cathodic response from this reaction was not observed on the backward scan analogous as in Reference [70]. Hence, successive cycles show that the oxidized Ni surface still enhances the oxidation of glucose and gluconolactone at more positive potential values (Figure 5c, dashed lines). Processes occurring at the Ni/Ti catalyst both in the 0.1 M NaOH solution (Figure 5c) and in that containing 0.1 M glucose (Figure 5c) are attributed to the reversible transformation of Ni(II)/Ni(III) in an alkaline media and glucose oxidation to gluconolactone by NiOOH , given that $\text{Ni(OH)}_2/\text{NiOOH}$ acts as an electron transfer [71–74]. The overall process of glucose oxidation on the Ni/Ti catalyst can be presented by the Equations (6) and (7):

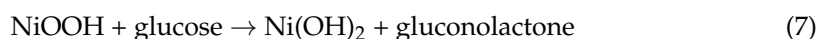
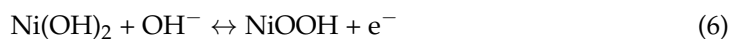
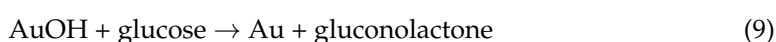


Figure 5b,d show CV curves of Mo/Ti and Ni/Ti catalysts, decorated with Au nanoparticles recorded in an aqueous solution of 0.1 M NaOH (solid line) and in that containing 0.1 M glucose (dashed line) at 25 °C with a scan rate of 50 mV s^{-1} . The modification of both catalysts with Au results in the formation of typical glucose oxidation peaks similar to those found on bare Au electrodes and can be characterized by the same processes occurring on bare Au catalysts. However, the CVs determined on both catalysts differ considerably not only in the values of peak currents and onset potentials but also in the ratio (I/II) of peak I to peak II of the glucose and gluconolactone oxidation currents, respectively.

The first scans of CVs on Au(Ni)/Ti and Au(Mo)/Ti electrodes presented in Figure 5f clearly indicate that glucose electrooxidation onset potential on the Au(Ni)/Ti catalyst appears at a considerably lower potential of ca. -0.688 V (E_{onset} is ca. -0.43 V on Au(Mo)/Ti) and gives significantly higher current density values compared to those obtained on the Au(Mo)/Ti catalyst. They are also much higher than the oxidation currents determined on Au-unmodified Mo/Ti and Ni/Ti catalysts (Figure 5e). The increase in current densities on Au-modified Ni/Ti and Mo/Ti catalysts can be attributed not only to the synergistic effect between mentioned elements but also to the number of AuOH_{ads} active sites formed by chemisorption of OH^- anions in an alkaline medium. Analogous to glucose oxidation on the bare Au catalyst, glucose oxidation on Au(Ni)/Ti and Au(Mo)/Ti highly depends on the number of available OH_{ads} to form active sites. A limited number of $\text{Au-OH}_{\text{ads}}$ sites results in the accumulation of intermediate products that block the active sites of the catalyst surface and lead to a current decrease. The values of the glucose oxidation current peaks I and II on the Au(Ni)/Ti catalyst are equal to ca 3.60 and 4.14 mA cm^2 and are ca. 20.5 and 4.8 times higher than those found on the Au(Mo)/Ti catalyst, which equal to 0.18 and 0.86 mA cm^{-2} , respectively. Furthermore, the current peak I/II ratios of the Au(Ni)/Ti and Au(Mo)/Ti catalysts are 0.87 and 0.21 , correspondingly indicating that the processes in the potential regions of these peaks, i.e., the electrooxidation of glucose and gluconolactone, occur at a relatively similar rate on the Au(Ni)/Ti catalyst, while the oxidation of gluconolactone is predominant on the Au(Mo)/Ti catalyst. Notably, the Au(Ni)/Ti favors glucose oxidation, pointing to the fact that possibly higher Au loading of 4.1 $\mu\text{g}_{\text{Au}} \text{cm}^{-2}$ in the catalyst composition compared to that of 1.2 $\mu\text{g}_{\text{Au}} \text{cm}^{-2}$ in Au(Mo)/Ti is responsible for the

higher availability of AuOH_{ads} active sites formed on the catalyst surface that are required for glucose oxidation. The increase in Au loading results in higher current densities at both peaks and more negative values for the onset potential of the Au(Ni)/Ti catalyst compared to those at Au(Mo)/Ti. Such findings are additionally supported by the CVs of the above catalysts recorded in 0.1 M NaOH, which show almost no current density response on the Au(Mo)/Ti catalyst, whereas on the Au(Ni)/Ti catalyst, the typical peaks on Au- and Ni-based electrodes in alkaline solutions are observed (Figure 5b,d). The proposed glucose oxidation on the Au(Ni)/Ti catalyst consists of its electrooxidation by Ni(III) according to Equations (6) and (7) and by Au(I) according to Equations (8) and (9) [75] as follows:



In addition, it should be noted that the CV curves for both Au-modified catalysts show an increase in current with the number of cycles and reach stable values quite quickly (Figure 5b,d), in contrast to the current values observed on the Au-unmodified Mo/Ti and Ni/Ti catalysts (Figure 5a,c), indicating relatively good electrocatalytic stability and activity of both Au(Mo)/Ti and Au(Ni)/Ti catalysts in the electrooxidation of glucose.

The electrocatalytic activity towards GOR of the coupled NiMo/Ti catalysts with different total metal loadings of 15.6, 40.0, and 45.0 $\mu\text{g cm}^{-2}$ for NiMo/Ti-1, NiMo/Ti-2, and NiMo/Ti-3, respectively, was investigated for GOR also. Their electrocatalytic activities were compared with those of Au-modified catalysts having almost similar total metal loadings of 15.4, 39.0, and 42.5 $\mu\text{g cm}^{-2}$ and similarly denoted as Au(NiMo)/Ti-1, Au(NiMo)/Ti-2, and Au(NiMo)/Ti-3, respectively. The detailed loadings of the relevant metals in the catalysts are given in Table 1, which demonstrates that the separate metal loadings of the correspondingly labeled Au-modified and Au-unmodified catalysts are very close. The analysis of CVs for the electrooxidation of glucose on the NiMo/Ti-1, NiMo/Ti-2, and NiMo/Ti-3 catalysts presented in Figure 6a,c,e shows that the peak current density values during the first cycle are rather close and are in the ranges from ca. 0.60 to ca. 0.69 mA cm^{-2} , regardless of the increase in the total catalyst loading. Meanwhile, the onset potential for the same catalysts shifts to more negative potential values from ca. -0.42 V to -0.50 V, with an increase in total catalyst loading from 15.4 to 42.5 $\mu\text{g cm}^{-2}$. At the same time, a hardly pronounced current hump develops, which is more clearly visible on these catalysts in the positive potential scans recorded in a solution of 0.1 M NaOH containing 0.1 M glucose (Figure 7a, 1st cycles). The values of the current density on the NiMo/Ti-1, NiMo/Ti-2, and NiMo/Ti-3 catalysts are higher than those on the Mo/Ti catalyst and lower than those on the Ni/Ti catalyst, indicating that the electrooxidation of glucose on these catalysts is dependent on the increase in the total catalyst loading, which is mainly related to the increase in Ni amount (Table 1). The Ni loadings in the NiMo/Ti-1, NiMo/Ti-2, and NiMo/Ti-3 catalysts are 13.5, 35.7, and 39.3 $\mu\text{g}_{\text{Ni}} \text{cm}^{-2}$, respectively, whereas the Mo loadings are only 2.4, 4.3, and 5.7 $\mu\text{g}_{\text{Mo}} \text{cm}^{-2}$. The low loading of Ni of ca. 13.5 $\mu\text{g}_{\text{Ni}} \text{cm}^{-2}$ in the NiMo/Ti-1 catalyst can be related to an insufficient number of active sites formed for glucose oxidation leading to the accumulation of reaction intermediates, which results in the disappearance of the current hump and lower current values obtained with a shift of the onset potential towards more negative values. These assumptions are in line with the CVs recorded in the background solution of 0.1 M NaOH on the NiMo/Ti-1 catalyst, confirming the absence of the typical red/ox peaks required for the transformation of Ni(II)/Ni(III) in an alkaline medium to produce the Ni(III) species necessary for glucose electrooxidation (Figure 6a).

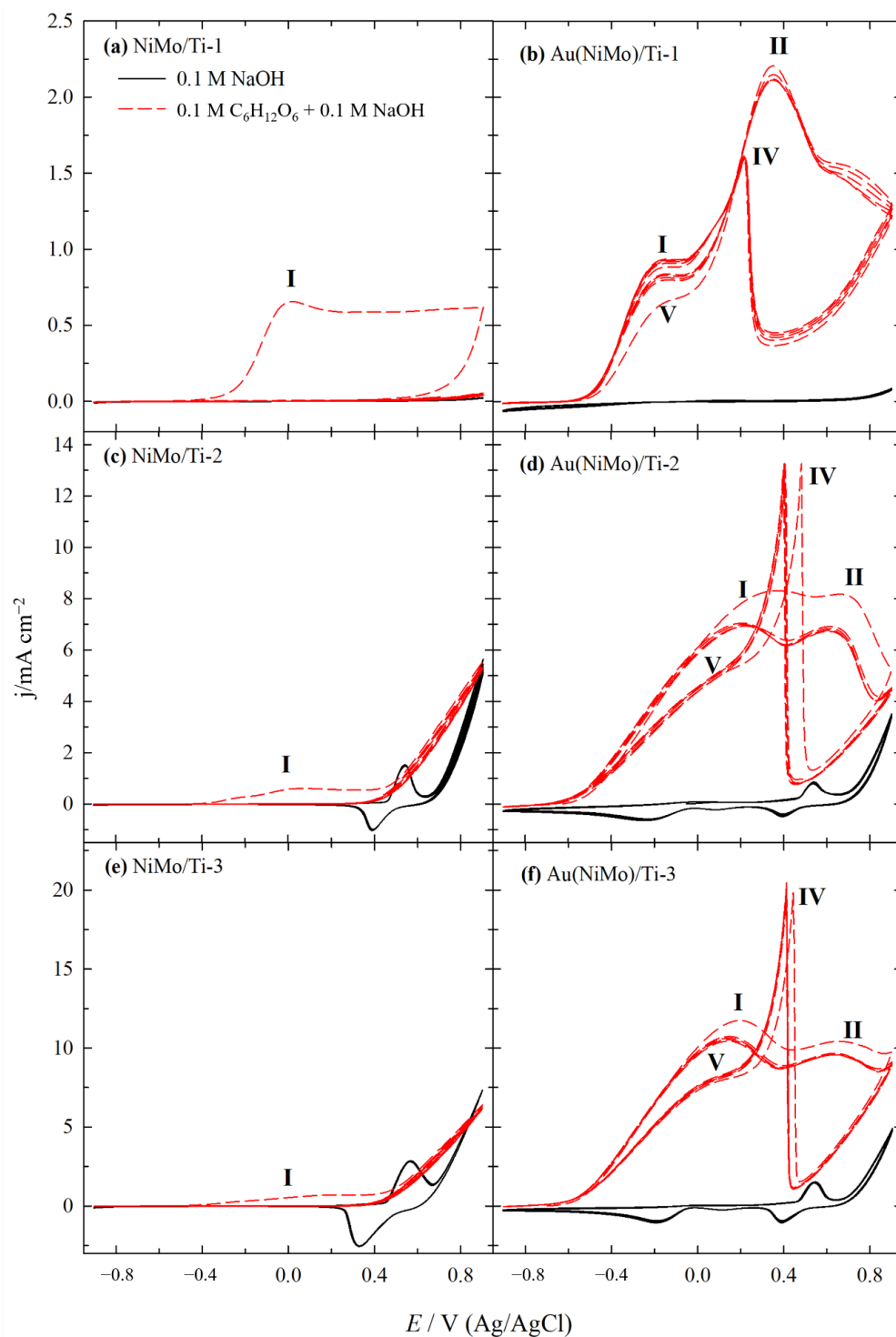


Figure 6. Cyclic voltammograms recorded on NiMo/Ti (a,c,e) and Au(NiMo)/Ti (b,d,f) catalysts in the 0.1 M NaOH solution (solid line) and that containing 0.1 M glucose (dashed line) at 25 °C at an electrode potential scan rate of 50 mV s⁻¹.

Notably, successive cycles for glucose electrooxidation lead to a sharp decrease in current, indicating that the NiMo/Ti-1 catalyst becomes inactive towards glucose electrooxidation. These findings are further supported by the SEM analysis (Figure 2a), which shows that a porous structure was not formed on the NiMo/Ti-1 catalyst. Due to insufficient Ni loading, only randomly distributed spherical particles were observed on the surface of the

NiMo/Ti-1 catalyst. It is evident that forming a porous structure is an additional factor significantly contributing to faster GOR.

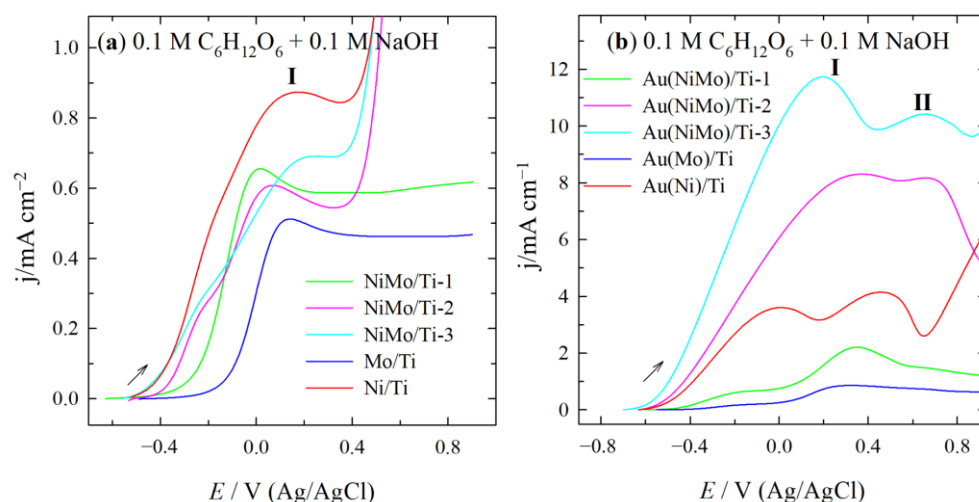


Figure 7. Positive-going potential scans (1st cycles) of: (a) Ni/Ti, Mo/Ti, NiMo/Ti-1, NiMo/Ti-2, and NiMo/Ti-3; (b) Au(Ni)/Ti, Au(Mo)/Ti, Au(NiMo)/Ti-1, Au(NiMo)/Ti-2, and Au(NiMo)/Ti-3 catalysts in 0.1 M $C_6H_{12}O_6$ + 0.1 M NaOH at 25 °C at an electrode potential scan rate of 50 $mV s^{-1}$.

In contrast, all Au-modified NiMo/Ti catalysts showed good activity for glucose electrooxidation, with a relatively stable CV already after the second cycle (Figure 6b,d,f). The presence of Au in the NiMo/Ti catalyst obviously improves the stability of the catalyst. A strong increase in current is also observed with the formation of two gold-specific peaks with different peak ratios (I/II), which depend on the catalyst loading used. A summary of electrochemical measurements of CVs at different catalysts in 0.1 M NaOH + 0.1 M $C_6H_{12}O_6$ at 25 °C and a potential scan rate of 50 $mV s^{-1}$ is presented in Table 2.

Table 2. Summary of electrochemical measurements (1st cycle of CV) at different catalysts in 0.1 M NaOH + 0.1 M $C_6H_{12}O_6$ at 25 °C and a potential scan rate of 50 $mV s^{-1}$.

Catalyst	E_{onset}/V	Peak I		Peak II		Peak Ratio (I/II)
		E/V	$j/mA cm^{-2}$	E/V	$j/mA cm^{-2}$	
Au(MoTi)/Ti-1	−0.537	−0.099	0.68	0.349	2.21	0.31
Au(MoTi)/Ti-2	−0.619	0.362	8.30	0.660	8.17	1.02
Au(MoTi)/Ti-3	−0.684	0.197	11.73	0.650	10.42	1.13
AuNi/Ti	−0.430	0.001	3.60	0.474	4.14	0.87
AuMo/Ti	−0.688	−0.171	0.18	0.322	0.86	0.21

For stabilized CVs recorded on Au(NiMo)/Ti-1, Au(NiMo)/Ti-2, and Au(NiMo)/Ti-3 with total metal loadings of 15.4, 39.0, and 42.5 $\mu g cm^{-2}$, the (I/II) ratios are 0.31, 1.02, and 1.13, respectively. It should be noted that the increase in the current peak ratio (I/II) value correlates with an increase in Au loadings that are ca. 1.8, 2.3, and 4.5 $\mu g_{Au} cm^{-2}$ for the above-mentioned catalysts. The increasing character of the current peak ratio (I/II) clearly shows that the electrooxidation of glucose and gluconolactone proceeds at a relatively similar rate on the Au(NiMo)/Ti-2 catalyst, suggesting that the surface of the catalyst seems to be equally active for the electrooxidation of glucose and gluconolactone. Moreover, the electrooxidation of glucose on the Au(NiMo)/Ti-3 catalyst proceeds slightly faster due to the higher Au loading (ca. 4.5 $\mu g_{Au} cm^{-2}$), indicating a presence of a sufficient number of active sites required for GOR.

A comparison of 1st cycles of positive-going potential scans characterizing the activity of the catalyst for GOR is presented in Figure 7.

They demonstrate that the highest current values and the lowest onset potential are observed at the Au(NiMo)/Ti-3 catalyst as compared to those of Au(Mo)/Ti, Au(Ni)/Ti, Au(NiMo)/Ti-1, and Au(NiMo)/Ti-2 with total catalyst loadings of ca. 5.3, 64.0, 15.4, and 39.0, respectively. The Au(NiMo)/Ti-3 catalyst gives 65.2, 3.3, 17.5, and 1.4 times higher current density values in the potential region of peak I and 12.2, 2.5, 4.7, and 1.3 times, respectively, higher current density values for the potential region of peak II as compared to those values obtained at the Au(Mo)/Ti, Au(Ni)/Ti, Au(NiMo)/Ti-1, and Au(NiMo)/Ti-2 catalysts, respectively.

The highest activity and stability of all Au-modified NiMo/Ti catalysts for GOR can be attributed to the modification of the NiMo/Ti catalyst by Au, which stabilizes the catalyst considerably as well as to the synergy between the Au and porous NiMo coating deposited on the Ti surface. The developed porous surface with open spaces containing a large number of active sites and the relatively wide flow channels within the porous structure allow easy diffusion of the electrolyte, and easy electron transfer, which all contribute to facilitating GOR.

In order to evaluate the electrocatalytic activity of the investigated catalysts towards GOR, the current density values were normalized in reference to Au loadings for each catalyst in alkaline media (Figure 8). The specific mass-current density of the Au(NiMo)/Ti-2 catalyst was found to be 6.6 and 1.1 times higher than that of the Au(NiMo)/Ti-1 and Au(NiMo)/Ti-3 catalysts for peak I, respectively. Meanwhile, in the case of peak II, the specific mass-current density of the Au(NiMo)/Ti-2 catalyst was 2.5 and 1.2 times higher than the catalysts mentioned above, respectively.

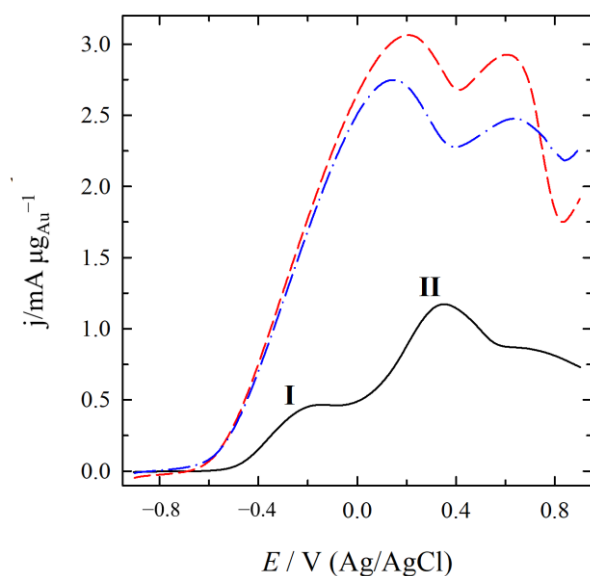


Figure 8. Au loading-normalized stabilized anodic scans recorded on Au(NiMo)/Ti-1, Au(NiMo)/Ti-2, and Au(NiMo)/Ti-3 catalysts in 0.1 M $C_6H_{12}O_6$ + 0.1 M NaOH at 25 °C at an electrode potential scan rate of 50 mV s⁻¹.

2.3. Direct Alkaline $C_6H_{12}O_6$ - H_2O_2 Single Fuel Cell Tests

Direct alkaline $C_6H_{12}O_6$ - H_2O_2 single fuel cell tests were carried out by employing the prepared NiMo/Ti and Au(NiMo)/Ti coatings (with a geometric area of 2 cm²) as the anode and a Pt plate as the cathode (Figures 9 and 10).

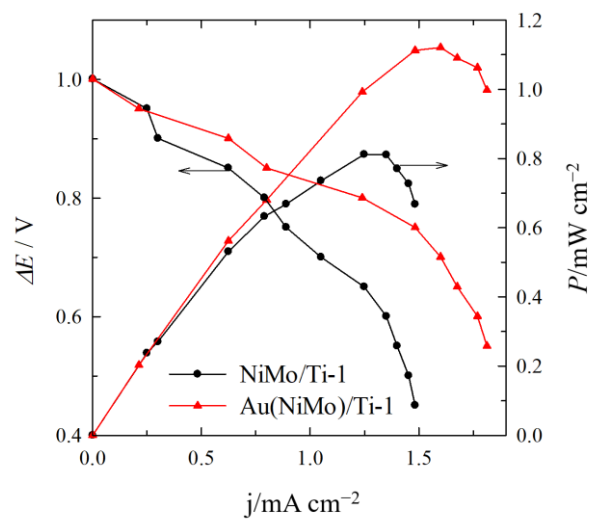


Figure 9. Cell polarization and power density curves for the $C_6H_{12}O_6$ - H_2O_2 fuel cell using NiMo/Ti-1 and Au(NiMo)/Ti-1 anode coatings with anolyte consisted of 0.1 M $C_6H_{12}O_6$ + 1 M NaOH and 5 M H_2O_2 + 1.5 M HCl catholyte at 25 °C.

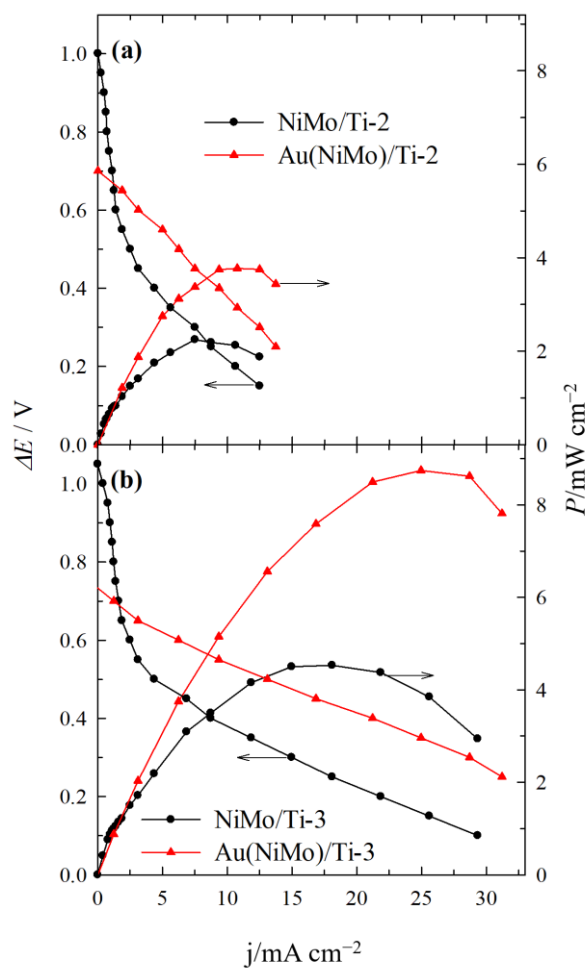


Figure 10. Cell polarization and power density curves for the $C_6H_{12}O_6$ - H_2O_2 fuel cell using NiMo/Ti-2 (a), NiMo/Ti-3 (b), Au(NiMo)/Ti-2 (a), and Au(NiMo)/Ti-3 (b) anode coating with anolyte consisted of 0.1 M $C_6H_{12}O_6$ + 1 M NaOH and 5 M H_2O_2 + 1.5 M HCl catholyte at 25 °C.

The anolyte was composed of an alkaline mixture of 0.1 M $C_6H_{12}O_6$ + 1 M NaOH and the catholyte contained 5 M H_2O_2 + 1.5 M HCl at a temperature of 25 °C. The performance of the fuel cell was evaluated by recording the cell polarization and obtaining the corresponding power density curves. Figures 9 and 10 present the fuel cell polarization curves and the corresponding power densities against the current density by employing the NiMo/Ti and Au(NiMo)/Ti catalysts at 25 °C. Notably, peak power density values were from 1.4 to 1.9 times higher when using the Au(NiMo)/Ti catalyst as an anode material than NiMo/Ti (Table 3). It was found that the highest peak power densities up to 8.75 mW cm^{-2} were attained at 25 °C using the Au(NiMo)/Ti-3 catalyst, with the Au loading of $3.9 \text{ } \mu\text{g cm}^{-2}$. The peak power density values were 7.8 times higher when using the Au(NiMo)/Ti-3 catalyst as an anode material than Au(NiMo)/Ti-1. The highest specific peak power densities of $2.24 \text{ mW } \mu\text{g}_{\text{Au}}^{-1}$ at 25 °C were attained using the Au(NiMo)/Ti-3 anode with the Au loading of $3.9 \text{ } \mu\text{g cm}^{-2}$. The specific peak power density achieved using the Au(NiMo)/Ti-3 anode was 1.4 and 3.6 times higher than the specific peak power density obtained using Au(NiMo)/Ti-2 and Au(NiMo)/Ti-1 anodes, respectively.

Table 3. Electrochemical parameters of $C_6H_{12}O_6$ - H_2O_2 using different NiMo/Ti and Au(NiMo)/Ti anode catalysts.

Catalyst	<i>E</i> at Peak Power Density (V)	<i>j</i> at Peak Power Density (mA cm^{-2})	Peak Power Density (mW cm^{-2})	Specific Peak Power Density (mW $\mu\text{g}_{\text{Au}}^{-1}$)
NiMo/Ti-1	0.65	1.25	0.81	-
Au(NiMo)/Ti-1	0.70	1.60	1.12	0.62
NiMo/Ti-2	0.30	7.49	2.25	-
Au(NiMo)/Ti-2	0.35	10.76	3.77	1.64
NiMo/Ti-3	0.25	18.10	4.53	-
Au(NiMo)/Ti-3	0.35	24.97	8.75	2.24

3. Materials and Methods

3.1. Chemicals

Titanium (Ti) plate (99.7% pure, Sigma-Aldrich, Saint Louis, MO, USA), $\text{HAuCl}_4 \cdot$ (99.99%, ≥ 49.0 % Au, Sigma-Aldrich, Saint Louis, MO, USA), $C_6H_{12}O_6$ (D-(+)-glucose, 99.5%, Sigma-Aldrich, Saint Louis, MO, USA); NaOH (98.8%, Chempur, Karlsruhe, Germany), H_2SO_4 (96%, Eurochemicals, Vilnius, Lithuania), HCl (Chempur, 35–38 %, Karlsruhe, Germany), HNO_3 (67%, Eurochemicals, Vilnius, Lithuania), NiSO_4 (99%, Sigma-Aldrich, Saint Louis, MO, USA) and Na_2MoO_4 (98%, Sigma-Aldrich, Saint Louis, MO, USA), H_2O_2 (Merck, 35 wt.%, Rahway, NJ, USA), were used as received and all solutions were prepared using deionized (Elix 3 Millipore, Merck, Rahway, NJ, USA) water. All chemicals were of analytical grade. A Nafion® N117 membrane was purchased from DuPont (Wilmington, DE, USA).

3.2. Fabrication of Catalysts

The catalysts were prepared by a two-step process that involved electrodeposition of Ni, Mo, and NiMo coatings on the surface of the Ti plates (1×1 cm) followed by a spontaneous Au displacement from the Au(III)-containing solution. Prior to the deposition of the 3D NiMo, Ni, and Mo coatings, the Ti plates were pretreated in H_2SO_4 (1:1 vol) solution at 70 °C for 3 s. The composition of plating baths and parameters for the deposition of Ni, Mo, and NiMo coatings on Ti are given in Table 4. For the deposition of different NiMo coatings, the concentration of Na_2MoO_4 was kept constant, whereas the concentration of NiSO_4 was varied (Table 4). The coatings were plated at the current of 0.1 A followed by the current of 1 A for 3 min at each current. The obtained coatings were named as Ni/Ti, Mo/Ti, NiMo/Ti-1, NiMo/Ti-2, and NiMo/Ti-3. After that, the prepared coatings were decorated with Au crystallites by their immersion into a 1 mM HAuCl_4 + 0.1 M HCl solution for 10 s at a temperature of 25 °C. After plating, the samples were taken out, thoroughly rinsed

with deionized water, and air-dried at room temperature. Then, the prepared Au(Ni)/Ti, Au(Mo)/Ti, Au(NiMo)/Ti-1, Au(NiMo)/Ti-2, and Au(NiMo)/Ti-3 catalysts were used for measurements of the electrooxidation of glucose in an alkaline medium without any further treatment.

Table 4. The composition of plating baths and parameters for the deposition of Ni, Mo, and NiMo coatings.

Catalyst	Plating Bath Composition				Plating Parameters				
	NiSO ₄ , M	Na ₂ MoO ₄ , M	H ₂ SO ₄ , M	HCl, M	I ₁ , A	t ₁ , min	I ₂ , A	t ₂ , min	T, °C
Ni/Ti	0.5	-							
Mo/Ti	-	0.01							
NiMo/Ti-1	0.01	0.01	1.5	1.0	0.1	3	1.0	3	25
NiMo/Ti-2	0.1	0.01							
NiMo/Ti-3	0.5	0.01							

3.3. Characterization of Catalysts

The morphology and composition of the fabricated catalysts were characterized using a SEM workstation SEM TM 4000 Plus (HITACHI, Tokyo, Japan) with an energy dispersive X-ray (EDX) spectrometer (HITACHI, Tokyo, Japan). The Au loading in the prepared catalysts was estimated using an ICP optical emission spectrometer Optima 7000DV (Perkin Elmer, Waltham, MA, USA). The electrocatalytic activity of the as-prepared Ni/Ti, Au(Ni)/Ti, Mo/Ti, Au(Mo)/Ti, NiMo/Ti, and Au(NiMo)/Ti catalysts for GOR was investigated using the method of cyclic voltammetry. A standard thermostatic three-electrode electrochemical cell with a working volume of about 100 ml was used for electrochemical measurements. The Pt plate (1.0 × 1.0 cm) was used as a counter electrode. The Ag/AgCl in 3 M KCl was used as a reference electrode. The electrocatalytic activity of the designed Ni/Ti, Au(Ni)/Ti, Mo/Ti, Au(Mo)/Ti, NiMo/Ti, and Au(NiMo)/Ti catalysts was evaluated for GOR by recording cyclic voltammograms (CVs) in a 0.1 M C₆H₁₂O₆ + 0.1 M NaOH solution in the potential range from −0.9 to 0.9 V vs. Ag/AgCl at an electrode potential scan rate of 50 mV s^{−1}. The bulk Au electrode with a geometric area of 0.13 cm² was used for the comparison. All solutions were deaerated with argon (Ar) for 15 minutes before electrochemical measurements.

3.4. Fuel Cell Test Experiments

C₆H₁₂O₆-H₂O₂ tests were carried out by employing the NiMo/Ti and Au(NiMo)/Ti coatings with a geometric area of 2 cm² as the anode and a Pt plate with a geometric area of 3 cm² as the cathode. Each compartment of the cell contained 100 mL of the corresponding aqueous electrolyte. The anolyte was composed of an alkaline mixture of 0.1 M C₆H₁₂O₆ + 1 M NaOH and the catholyte contained 5 M H₂O₂ + 1.5 M HCl. A Nafion[®] N117 membrane was used to separate the anodic and cathodic compartments of the single direct C₆H₁₂O₆-H₂O₂ fuel cell. The membrane active area was ca. 30 cm². Cell measurements were conducted using a Zennium electrochemical workstation (ZAHNER-Elektrok GmbH & Co. KG, Kronach, Germany). The performance of the fuel cell was evaluated by recording the cell polarization curves. The load was applied in steps of 50 mV. Each step lasted 30 s (one point per second) and the cell voltage was continuously applied from one value to the next without disconnecting the cell. Power density values were calculated from the applied cell voltage and steady-state current. The presented current and peak power densities were normalized with respect to the geometric area of catalysts.

4. Conclusions

NiMo/Ti and Au(NiMo)/Ti catalysts with well-defined open-porous network structures were successfully prepared using electrodeposition and galvanic displacement techniques. The modification of NiMo/Ti catalysts with small amounts of Au (i.e., 1.8, 2.3, and

3.9 $\mu\text{g}_{\text{Au}} \text{cm}^{-2}$) improved the stability of the catalysts and led to significant enhancement of the catalysts' performance in terms of the lower onset potential and higher anodic peak currents in the electrooxidation of glucose. The excellent electrochemical properties of all as-prepared Au(NiMo)/Ti catalysts for glucose oxidation reaction are attributed to the synergy between the Au and the porous NiMo coating deposited on the Ti surface, as well as to the development of a porous surface structure with multiple open channels containing a large number of active sites facilitating the diffusion of the electrolyte and the transfer of electrons. The Au(NiMo)/Ti-3 anode with Au loading of 3.9 $\mu\text{g}_{\text{Au}} \text{cm}^{-2}$ in a constructed direct glucose-hydrogen peroxide ($\text{C}_6\text{H}_{12}\text{O}_6\text{-H}_2\text{O}_2$) single fuel cell demonstrated the highest electrocatalytic activity for glucose oxidation. It was found that the highest peak power density up to 8.75 mW cm^{-2} and the highest specific peak power density of 2.24 $\text{mW } \mu\text{g}_{\text{Au}}^{-1}$ were attained at 25 °C using the Au(NiMo)/Ti-3 catalyst with the Au loading of 3.9 $\mu\text{g cm}^{-2}$. The as-prepared porous Au(NiMo)/Ti catalyst appears to be a promising anode material for application in direct glucose fuel cells.

Author Contributions: Conceptualization, A.B., D.U., L.T.-T. and E.N.; methodology, D.U., J.V. and A.A.; formal analysis, D.U., J.V. and A.A.; investigation, D.U., A.A., A.B. and D.Š.; writing—original draft preparation, D.U. and A.B.; writing—review and editing, D.Š., L.T.-T. and E.N.; visualization, D.U., D.Š. and L.T.-T. All authors have read and agreed to the published version of the manuscript.

Funding: This research was funded by the European Social Fund under Measure No. 09.3.3-LMT-K-712-19-0138 'Development of Competences of Scientists, other Researchers and Students through Practical Research Activities'.

Data Availability Statement: Not applicable.

Conflicts of Interest: The authors declare no conflict of interest.

References

1. Kerzenmacher, S.; Ducrée, J.; Zengerle, R.; Stetten, F. Energy harvesting by implantable abiotically catalyzed glucose fuel cells. *J. Power Sources* **2008**, *182*, 1–17. [[CrossRef](#)]
2. Singh, R.; Kaur, N.; Singh, M. Bio-compatible bio-fuel cells for medical devices. *Mater. Today Proc.* **2021**, *44*, 242–249. [[CrossRef](#)]
3. Xu, Q.; Zhang, F.; Xu, L.; Leung, P.; Yang, C.; Li, H. The applications and prospect of fuel cells in medical field: A review. *Renew. Sustain. Energy Rev.* **2017**, *67*, 574–580. [[CrossRef](#)]
4. Ahmed, S.F.; Mofijur, M.; Islam, N.; Parisa, T.A.; Rafa, N.; Bokhari, A.; Klemeš, J.J.; Meurah, T.; Mahlia, I. Insights into the development of microbial fuel cells for generating biohydrogen, bioelectricity, and treating wastewater. *Energy* **2022**, *254*, 124163. [[CrossRef](#)]
5. Tung, S.-P.; Huang, T.-K.; Lee, C.-Y.; Chiu, H.-T. Electrochemical growth of gold nanostructures on carbon paper for alkaline direct glucose fuel cell. *RSC Advances* **2012**, *2*, 1068–1073. [[CrossRef](#)]
6. Basu, D.; Basu, S. Performance studies of Pd-Pt and Pt-Pd-Au catalyst for electrooxidation of glucose in direct glucose fuel cell. *Int. J. Hydrogen Energy* **2012**, *37*, 4678–4684. [[CrossRef](#)]
7. Chen, C.; Lin, C.; Chen, L. Functionalized carbon nanomaterial supported palladium nano-catalysts for electrocatalytic glucose oxidation reaction. *Electrochim. Acta* **2015**, *152*, 408–416. [[CrossRef](#)]
8. Yan, L.; Brouzgou, A.; Meng, Y.; Xiao, M.; Tsiakaras, P.; Song, S. Efficient and poison-tolerant PdAu/C binary electrocatalysts for glucose electrooxidation in alkaline medium. *Appl. Catal. B Environ.* **2014**, *150–151*, 268–274. [[CrossRef](#)]
9. Li, X.; Du, X. Molybdenum disulfide nanosheets supported Au-Pd bimetallic nanoparticles for non-enzymatic electrochemical sensing of hydrogen peroxide and glucose. *Sens. Actuators B Chem.* **2017**, *239*, 536–543. [[CrossRef](#)]
10. Gumilar, G.; Kaneti, Y.V.; Henzie, J.; Chatterjee, S.; Na, J.; Yulianto, B.; Nugraha, N.; Patah, A.; Bhaumik, A.; Yamauchi, Y. General synthesis of hierarchical sheet/plate-like M-BDC (M = Cu, Mn, Ni, and Zr) metal-organic frameworks for electrochemical non-enzymatic glucose sensing. *Chem. Sci.* **2020**, *11*, 3644–3655. [[CrossRef](#)]
11. Tang, X.; Zhang, B.; Xiao, C.; Zhou, H.; Wang, X.; He, D. Carbon nanotube template synthesis of hierarchical NiCoO₂ composite for non-enzyme glucose detection. *Sens. Actuators B Chem.* **2016**, *222*, 232–239. [[CrossRef](#)]
12. Jafarian, M.; Forouzandeh, F.; Danaee, I.; Gobal, F.; Mahjani, M.G. Electrocatalytic oxidation of glucose on Ni and NiCu alloy. *J. Solid State Electrochem.* **2009**, *13*, 1171–1179. [[CrossRef](#)]
13. Kung, C.; Cheng, Y.; Ho, K. Single layer of nickel hydroxide nanoparticles covered on a porous Ni foam and its application for highly sensitive non-enzymatic glucose sensor. *Sens. Actuators B Chem.* **2014**, *204*, 159–166. [[CrossRef](#)]
14. Zhao, Y.; Liu, X.; Wang, X.; Zhang, P.; Shi, J. Peony petal-like 3D graphene-nickel oxide nanocomposite decorated nickel foam as high-performance electrocatalyst for direct glucose alkaline fuel cell. *Int. J. Hydrogen Energy* **2017**, *42*, 29863–29873. [[CrossRef](#)]

15. Geng, D.; Bo, X.; Guo, L. Ni-doped molybdenum disulfide nanoparticles anchored on reduced graphene oxide as novel electroactive material for a non-enzymatic glucose sensor. *Sens. Actuators B* **2017**, *244*, 131–141. [[CrossRef](#)]
16. Shu, Y.; Li, B.; Chen, J.; Xu, Q.; Pang, H.; Hu, X. Facile synthesis of ultrathin nickel–cobalt phosphate 2D nanosheets with enhanced electrocatalytic activity for glucose. *ACS Appl. Mater. Interfaces* **2018**, *10*, 2360–2367. [[CrossRef](#)] [[PubMed](#)]
17. Gao, X.; Feng, W.; Xu, Y.; Jiang, Y.; Huang, C.; Yi, Y.; Guo, A.; Qiu, X.; Chen, W. Nickel catalysts supported on acetylene black for high-efficient electrochemical oxidation and sensitive detection of glucose. *Nanoscale Res. Lett.* **2020**, *17*, 23. [[CrossRef](#)] [[PubMed](#)]
18. Jeevanandham, G.; Jerome, R.; Murugan, N.; Preethika, M.; VEDIAPPAN, K.; Sundramoorthy, A.K. Nickel oxide decorated MoS₂ nanosheet-based non-enzymatic sensor for the selective detection of glucose. *RSC Adv.* **2020**, *10*, 643–650. [[CrossRef](#)]
19. Gao, M.; Liu, X.; Irfan, M.; Shi, J.; Wang, X.; Zhang, P. Nickel-cobalt composite catalyst-modified activated carbon anode for direct glucose alkaline fuel cell. *Int. J. Hydrogen Energy* **2018**, *43*, 1805–1815. [[CrossRef](#)]
20. Irfan, M.; Liu, X.; Li, S.; Khan, I.U.; Li, Y.; Wang, J.; Wang, X.; Du, X.; Wang, G.; Zhang, P. High-performance glucose fuel cell with bimetallic Ni–Co composite anchored on reduced graphene oxide as anode catalyst. *Renew. Energy* **2020**, *155*, 1118–1126. [[CrossRef](#)]
21. Jeevanandham, G.; VEDIAPPAN, K.; ALOTHMAN, Z.A.; Altalhi, T.; Sundramoorthy, A.K. Fabrication of 2D-MoSe₂ incorporated NiO Nanorods modified electrode for selective detection of glucose in serum samples. *Sci. Rep.* **2021**, *11*, 13266. [[CrossRef](#)] [[PubMed](#)]
22. Wang, F.; Feng, Y.; He, S.; Wang, L.; Guo, M.; Cao, Y.; Wang, Y.; Yu, Y. Nickel nanoparticles-loaded three-dimensional porous magnetic graphene-like material for non-enzymatic glucose sensing. *Microchem. J.* **2020**, *155*, 104748. [[CrossRef](#)]
23. Karimi-Maleh, H.; Cellat, K.; Arıkan, K.; Savk, A.; Karimi, F.; Şen, F. Palladium–Nickel nanoparticles decorated on Functionalized-MWCNT for high precision non-enzymatic glucose sensing. *Mater. Chem. Phys.* **2020**, *250*, 123042. [[CrossRef](#)]
24. Kirali, A.A.; Sreekantan, S.; Marimuthu, B. Fabrication of mesoporous carbon supported Ni–Mo catalysts for the enhanced conversion of glucose to ethylene glycol. *New J. Chem.* **2020**, *44*, 15958. [[CrossRef](#)]
25. Xu, F.; Wu, M.; Ma, G.; Xu, H.; Shang, W. Copper-molybdenum sulfide/reduced graphene oxide hybrid with three-dimensional wrinkles and pores for enhanced amperometric detection of glucose. *Microchem. J.* **2020**, *159*, 105432. [[CrossRef](#)]
26. Li, K.; Fan, G.; Yang, L.; Li, F. Novel ultrasensitive non-enzymatic glucose sensors based on controlled flower-like CuO hierarchical films. *Sens. Actuators B Chem.* **2014**, *199*, 175–182. [[CrossRef](#)]
27. Ci, S.; Wen, Z.; Mao, S.; Hou, Y.; Cui, S.; He, Z. Junhong Chen. One-pot synthesis of high-performance Co/graphene electrocatalysts for glucose fuel cells free of enzymes and precious metals. *Chem. Commun.* **2015**, *51*, 9354–9357. [[CrossRef](#)] [[PubMed](#)]
28. Yang, Z.; You, J. Synthesis of a three-dimensional porous Co₃O₄ network interconnected by MWCNTs and decorated with Au nanoparticles for enhanced nonenzymatic glucose sensing. *Colloids Surf. A Physicochem. Eng. Asp.* **2021**, *612*, 126064. [[CrossRef](#)]
29. Ye, Z.; Miao, R.; Miao, F.; Tao, B.; Paul, Y.Z.; Chu, K. 3D nanoporous core-shell ZnO@Co₃O₄ electrode materials for high-performance supercapacitors and nonenzymatic glucose sensors. *J. Electroanal. Chem.* **2021**, *903*, 115766. [[CrossRef](#)]
30. Khazraei, A.; Tarlani, A.; Eslami-Moghadam, M.; Muzart, J. New Bi₂MoO₆ nano-shapes toward ultrasensitive enzymeless glucose tracing: Synergetic effect of the Bi–Mo association. *Talanta* **2021**, *221*, 121560. [[CrossRef](#)]
31. Veerakumar, P.; Sangili, A.; Manavalan, S.; Thanasekaran, P.; Lin, K.-C. Research progress on porous carbon supported metal/metal oxide nanomaterials for supercapacitor electrode applications. *Ind. Eng. Chem. Res.* **2020**, *59*, 6347–6374. [[CrossRef](#)]
32. Hui, Y.; Wang, H.; Zuo, W.; Ma, X. Spider nest shaped multi-scale three-dimensional enzymatic electrodes for glucose/oxygen biofuel cells. *Int. J. Hydrogen Energy* **2022**, *47*, 6187–6199. [[CrossRef](#)]
33. Qiao, Z.; Yan, Y.; Bi, S. Three-dimensional DNA structures in situ decorated with metal nanoclusters for dual-mode biosensing of glucose. *Sens. Actuators B Chem.* **2022**, *352*, 131073. [[CrossRef](#)]
34. Yao, X.; Li, J.; Zhu, Y.; Li, L.; Zhang, W. Designed synthesis of three-dimensional callistemon-like networks structural multifunctional electrocatalyst: Graphitic-carbon-encapsulated Co nanoparticles/N-doped carbon nanotubes@carbon nanofibers for Zn-air batteries application. *Compos. Part B Eng.* **2020**, *193*, 108058. [[CrossRef](#)]
35. Yun, Q.; Lu, Q.; Zhang, X.; Tan, C.; Zhang, H. Three-dimensional architectures constructed from transition-metal dichalcogenide nanomaterials for electrochemical energy storage and conversion. *Angew. Chem.* **2018**, *57*, 626–646. [[CrossRef](#)] [[PubMed](#)]
36. Rong, S.; He, T.; Zhang, P. Self-assembly of MnO₂ nanostructures into high purity three-dimensional framework for high efficiency formaldehyde mineralization. *Appl. Catal. B Environ.* **2020**, *267*, 118375. [[CrossRef](#)]
37. Xiong, S.; Lin, M.; Wang, L.; Liu, S.; Weng, S.; Jiang, S.; Xu, Y.; Jiao, Y.; Chen, J. Defects-type three-dimensional Co₃O₄ nanomaterials for energy conversion and low temperature energy storage. *Appl. Surf. Sci.* **2021**, *546*, 149064. [[CrossRef](#)]
38. Snyder, J.; Asanithi, P.; Dalton, A.B.; Erlebacher, J. Stabilized nanoporous metals by dealloying ternary alloy precursors. *Adv. Mater.* **2008**, *20*, 4883–4886. [[CrossRef](#)]
39. Mott, D.; Luo, J.; Njoki, P.N.; Lin, Y.; Wang, L.; Zhong, C.J. Synergistic activity of gold-platinum alloy nanoparticle catalysts. *Catal. Today* **2007**, *122*, 378–385. [[CrossRef](#)]
40. Vega, A.A.; Newman, R.C. Nanoporous metals fabricated through electrochemical dealloying of Ag–Au–Pt with a systematic variation of Au to Pt ratio. *J. Electrochem. Soc.* **2014**, *161*, C1. [[CrossRef](#)]
41. Ruban, A.V.; Skriver, H.L.; Nørskov, J.K. Surface segregation energies in transition metal alloys. *Phys. Rev. B.* **1999**, *59*, 15990–115600. [[CrossRef](#)]
42. Vitos, L.; Ruban, A.V.; Skriver, H.L.; Kollar, J. The surface energy of metals. *Surf. Sci.* **1998**, *411*, 186–202. [[CrossRef](#)]

43. Nam, S.; Jo, H.; Choe, H.; Ahn, D.; Choi, H. Development of nanoporous copper foams by chemical dealloying of mechanically alloyed AlCu compounds. *Mater. Trans.* **2014**, *55*, 1414–1418. [[CrossRef](#)]
44. He, F.; Qiao, Z.; Qin, X.; Chao, L.; Tan, Y.; Xie, Q.; Yao, S. Dynamic gas bubble template electrodeposition mechanisms and amperometric glucose sensing performance of three kinds of three dimensional honeycomb-like porous nano-golds. *Sens. Actuators B. Chem.* **2019**, *296*, 126679. [[CrossRef](#)]
45. Li, Y.; Song, Y.Y.; Yang, C.; Xia, X.H. Hydrogen bubble dynamic template synthesis of porous gold for nonenzymatic electrochemical detection of glucose. *Electrochem. Commun.* **2007**, *9*, 981–988. [[CrossRef](#)]
46. Marozzi, C.A.; Chialvo, A.C. Development of electrode morphologies of interest in electrocatalysis: Part 2: Hydrogen evolution reaction on macroporous nickel electrodes. *Electrochim. Acta* **2001**, *46*, 861–866. [[CrossRef](#)]
47. Najdovski, I.; Selvakannan, P.R.; Bhargava, S.K.; O'Mullane, A.P. Formation of nanostructured porous Cu-Au surfaces: The influence of cationic sites on (electro)-catalysis. *Nanoscale* **2012**, *4*, 6298–6306. [[CrossRef](#)]
48. Reda, Y.; Abdel-Karim, R.; Zohdy, K.M.; El-Raghy, S. Electrochemical behavior of Ni–Cu foams fabricated by dynamic hydrogen bubble template electrodeposition used for energy applications. *Ain Shams Eng. J.* **2022**, *13*, 101532. [[CrossRef](#)]
49. Zeng, Y.; Ji, B.; Lv, Z.; Zheng, X.; Yang, X.; Cui, P.; Dong, Y.; Zhang, X.; Jiang, J. Rapid synthesis of porous Pt-Ni-Cu coatings with a wide composition range, tunable structures and enhanced electrocatalytic properties. *J. Alloys Compd.* **2020**, *835*, 155402. [[CrossRef](#)]
50. Eugénio, S.; Silva, T.M.; Carmezim, M.J.; Duarte, R.G.; Montemor, M.F. Electrodeposition and characterization of nickel-copper metallic foams for application as electrodes for supercapacitors. *J. Appl. Electrochem.* **2014**, *44*, 455–465. [[CrossRef](#)]
51. Shahryari, Z.; Gheisari, K.; Yeganeh, M.; Ramezanzadeh, B. Corrosion mitigation ability of differently synthesized polypyrrole (PPy-FeCl₃ & PPy-APS) conductive polymers modified with Na₂MoO₄ on mild steel in 3.5% NaCl solution: Comparative study and optimization. *Corrosion Sci.* **2021**, *193*, 109894.
52. Ferreira, G.C.A.; Napporn, T.W.; Kokoh, K.B.; Varela, H. Complex oscillatory kinetics in the electro-oxidation of glucose on gold. *J. Electrochem. Soc.* **2017**, *164*, H603. [[CrossRef](#)]
53. Upskuvienė, D.; Sukackienė, Z.; Balčiūnaitė, A.; Kepenienė, V.; Šimkūnaitė, D.; Šimkūnaitė-Stanyrienė, B.; Vaitkus, R.; Tamašauskaitė-Tamašiūnaitė, L.; Norkus, E. Investigation of glucose electrooxidation on Co and CoB alloy coatings modified with Au nanoparticles. *Chemija* **2019**, *30*, 23–32. [[CrossRef](#)]
54. Vassilyev, Y.B.; Khazova, O.A.; Nikolaeva, N.N. Kinetics and mechanism of glucose electrooxidation on different electrode-catalysts: Part II. Effect of the nature of the electrode and the electrooxidation mechanism. *J. Electroanal. Chem. Interfacial Electrochem.* **1985**, *196*, 127–144. [[CrossRef](#)]
55. Arjona, N.; Trejo, G.; Ledesma-García, J.; Arriaga, L.G.; Guerra-Balcázar, M. An electrokinetic-combined electrochemical study of the glucose electro-oxidation reaction: Effect of gold surface energy. *RSC Adv.* **2016**, *6*, 15630–15638. [[CrossRef](#)]
56. Pasta, M.; La Mantia, F.; Cui, Y. Mechanism of glucose electrochemical oxidation on gold surface. *Electrochim. Acta* **2010**, *55*, 5561–5568. [[CrossRef](#)]
57. Tominaga, M.; Shimazoe, T.; Nagashima, M.; Tani-Guchi, I. Electrocatalytic oxidation of glucose at gold nanoparticle-modified carbon electrodes in alkaline and neutral solutions. *Electrochem. Commun.* **2005**, *7*, 189–193. [[CrossRef](#)]
58. Jusys, Z.; Behm, R.J. The effect of anions and pH on the activity and selectivity of an annealed polycrystalline Au film electrode in the oxygen reduction reaction—Revisited. *ChemPhysChem* **2019**, *20*, 3276–3288. [[CrossRef](#)]
59. Brouzgov, A.; Tsiakaras, P. Electrocatalysts for Glucose Electrooxidation Reaction: A Review. *Top. Catal.* **2015**, *58*, 1311–1327. [[CrossRef](#)]
60. Arjona, N.; Guerra-Balcázar, M.; Trejo, G.; Ledesma-García, J.; Arriaga, L.G. Electrochemical growth of Au architectures on glassy carbon and their evaluation toward glucose oxidation reaction. *New J. Chem.* **2012**, *36*, 2555–2561. [[CrossRef](#)]
61. Escalona-Villalpando, R.A.; Gurrola, M.P.; Trejo, G.; Guerra-Balcázar, M.; Ledesma-García, J.; Arriaga, L.G. Electrodeposition of gold on oxidized and reduced graphite surfaces and its influence on glucose oxidation. *J. Electroanal. Chem.* **2018**, *816*, 92–98. [[CrossRef](#)]
62. Pourbaix, M. *Atlas of Electrochemical Equilibria in Aqueous Solutions*, 2nd ed.; NACE International: Houston, TX, USA, 1974.
63. Hull, M.N. The anodic oxidation of molybdenum in hydroxide ion solutions. *J. Electroanal. Chem.* **1971**, *30*, 1–3. [[CrossRef](#)]
64. Hull, M.N. On the anodic dissolution of molybdenum in acidic and alkaline electrolytes. *J. Electroanal. Chem.* **1972**, *38*, 143–157. [[CrossRef](#)]
65. Armstrong, R.D.; Bell, M.F.; Metcalfe, A.A. The anodic dissolution of molybdenum in alkaline solutions, electrochemical measurements. *J. Electroanal. Chem.* **1977**, *84*, 61–72. [[CrossRef](#)]
66. Badawy, W.A.; Al-Kharafi, F.M. Corrosion and passivation behaviors of molybdenum in aqueous solutions of different pH. *Electrochim. Acta* **1998**, *44*, 693–702. [[CrossRef](#)]
67. Badawy, W.A.; Feky, H.E.; Helal, N.H.; Mohammed, H.H. Cathodic hydrogen evolution on molybdenum in NaOH solutions. *Int. J. Hydrogen Energy* **2013**, *38*, 9625–9632. [[CrossRef](#)]
68. Rauscher, T.; Müller, C.I.; Schmidt, A.; Kieback, B.; Röntzsch, L. Ni-Mo-B alloys as cathode material for alkaline water electrolysis. *Int. J. Hydrogen Energy* **2016**, *41*, 2165–2176. [[CrossRef](#)]
69. Saji, V.S.; Lee, C.W. Molybdenum, Molybdenum Oxides, and their Electrochemistry. *ChemSusChem* **2012**, *5*, 1146–1161. [[CrossRef](#)] [[PubMed](#)]

70. Danial, A.S.; Saleh, M.M.; Salih, S.A.; Awad, M.I. On the synthesis of nickel oxide nanoparticles by sol-gel technique and its electrocatalytic oxidation of glucose. *J. Power Sources* **2015**, *293*, 101–108. [[CrossRef](#)]
71. Seghioyer, A.; Chevalet, J.; Barhoun, A.; Lantelme, F. Electrochemical oxidation of nickel in alkaline solutions: A voltammetric study and modelling. *J. Electroanal. Chem.* **1998**, *442*, 113–123. [[CrossRef](#)]
72. Lakhdari, D.; Guittoum, A.; Benbrahim, N.; Belgherbi, O.; Berkani, M.; Seid, L.; Khtar, S.A.; Saeed, M.A.; Lakhdari, N. Elaboration and characterization of Ni (NPs)-PANI hybrid material by electrodeposition for non-enzymatic glucose sensing. *J. Electron. Mater.* **2021**, *50*, 5250–5258. [[CrossRef](#)]
73. Chelaghmia, M.L.; Nacef, M.; Affoune, A.M.; Pontié, M.; Derabla, T. Facile synthesis of Ni(OH)₂ modified disposable pencil graphite electrode and its application for highly sensitive non-enzymatic glucose sensor. *Electroanalysis* **2018**, *30*, 1117–1124. [[CrossRef](#)]
74. Zhang, L.; Ding, Y.; Li, R.; Ye, C.; Zhao, G.; Wang, Y. Ni-Based metal–organic framework derived Ni@C nanosheets on a Ni foam substrate as a supersensitive non-enzymatic glucose sensor. *J. Mater. Chem. B* **2017**, *5*, 5549–5555. [[CrossRef](#)]
75. Qin, L.; He, L.; Zhao, J.; Zhao, B.; Yin, Y.; Yang, Y. Synthesis of Ni/Au multilayer nanowire arrays for ultrasensitive non-enzymatic sensing of glucose. *Sens. Actuators B* **2017**, *240*, 779–784. [[CrossRef](#)]